ELECTROTONIC STRUCTURE AND THE POTENTIAL FOR LOCAL COMPUTATION IN MOTORNEURONS OF THE STOMATOGASTRIC GANGLION OF THE CRAB Cancer borealis

Journal:	*The Journal of Comparative Neurology*
Manuscript ID:	draft
Manuscript Type:	Research Article
Date Submitted by the Author:	n/a
Keywords:	functional morphology, neuron tracing, crustacean, neurite

ELECTROTONIC STRUCTURE AND THE POTENTIAL FOR LOCAL COMPUTATION IN MOTORNEURONS OF THE STOMATOGASTRIC GANGLION OF THE CRAB *Cancer borealis*

Daniel K. Hartline[1*], Katherine Graubard[2] and Ann E. Wilensky[2,3]

[1]Békésy Laboratory of Neurobiology, Pacific Biomedical Research Center, University of Hawaii, Honolulu, HI 96822 USA

[2]Department of Biology, Box 351800, University of Washington, Seattle, WA 98195-1800 USA

[3] present address: Center for Neural Science, New York University, 4 Washington Place, Rm. 809, New York, NY, 10003 USA

31 text pages; 8 figures; 2 tables

Running head: Electrotonic structure of stomatogastric neurons

Associate Editor: Leslie Tolbert

Indexing terms: functional morphology, neuron tracing, crustacean, neurite

* Correspondence to: Daniel K. Hartline; phone: 808-956-8003; FAX: 808-956-6984;

email: danh@hawaii.edu

Support: NSF grants 96-04505 (D.H.) and 96-04693 (K.G.) and the Human Frontiers Science Program. Cell-fills supported by NIH NS15697 (K.G.).

ABSTRACT

An important current issue in cellular neurophysiology is determining the extent to which neurons, as a result of functional morphological properties, compute as single or multiple units of action. The extensive ramification of neurons in fine neuritic neuropilar structures having intermixed input and output synapses offers the possibility for local computation within restricted regions of the neuritic tree. To assess the potential for such in one of the better understood neural circuits, we examined passive properties of reconstructed VD motorneurons from the stomatogastric ganglion of the crab, *Cancer borealis,* using computer simulations. Input characteristics at the soma to both simulated current pulses and sinusoids resembled those of a sphere attached to an infinite cylinder ("ball and stick") in parallel with a short (λ=0.2) sealed cylinder. Despite the variable appearance of different VD cells, input characteristics for soma and axonal sites showed little variation (<13%). Voltage perturbations at the origin of a secondary neurite attenuated little in spreading to its most distal tips for all but the highest frequencies examined (1 kHz). However, attenuation along the primary neurites was markedly greater owing to loading by soma and axons. This produced a frequency-dependent gradient in signal strength along the primary neurites. Voltage spread from peripheral tips was highly attenuated at the primary trunk (up to 80% for DC), producing a substantial isolation between neurites that arise from different secondary processes. Contrasting with voltage attenuation, transfer-impedance between tips and more central points, or between different tips on different secondary branches, was relatively constant at low frequencies (< 10 Hz). We conclude that there is a potential for morphologically-derived segregation of output properties and local computation from different passive secondary trees within this STG neuron, while the disparity in passive input properties from the different trees affecting axonal sites is much less.

INTRODUCTION

The "Neuron Doctrine" holds that the functions of the nervous system are subsumed by a cellular type, the "neuron," which forms the substrate for information acquisition, conduction, processing and delivery. One of the long-held corollaries of this view is that the neuron is the primary functional unit of action of the nervous system: it receives diverse signals from input sources, integrates them with cellular properties and produces a synaptic output, through spike-mediated or non-spiking mechanisms (e.g. Bullock and Horridge 1965). It has been long-recognized, however, that neurons are computationally heterogeneous at the input: integration produced in a postsynaptic cell depends on the location of presynaptic terminals on the postsynaptic arbor (e.g. Rall 1962). Heterogeneity in output is found in neurons with multiple axons and semi-independent trigger zones (Otani and Bullock 1959; Tauc and Hughes 1963; Hartline 1967) or a mixture of spiking and non-spiking output modalities (Watanabe 1958; Maynard and Walton 1964). However, in most cases the output of a neuron is viewed as nearly unitary: the same or at least closely parallel at all output points. The discovery of dendrodendritic synapses (Rall et al 1966) and computational analysis of the regional spread of signals in dendritic (or more generally, neuritic) trees (Graubard and Calvin 1979) has changed that. It has given rise to the concept of "local computation:" the compartmentalization of inputs and outputs such that different regions of a neuron may receive and transmit different signals. Whether local computation is a significant feature of a given neuron is often not an easy issue to assess experimentally. Much depends on the extent to which electrotonic decrement in fine neurites might cause a partial isolation of different cell regions. Unfortunately, such fine neurites are not easy to record from with present technology. The issue is more amenable to study in simulations of neurons reconstructed realistically using modern morphometric techniques.

The stomatogastric ganglion (STG) of decapod crustaceans holds the distinction of being one of the better understood of all neural networks. How the morphological features of its cells

contribute to its computational characteristics is thus of particular interest. In order to assess possibilities for local computation in this simple motor pattern-generating network, we have investigated the computational properties of neurons belonging to one of the reidentifiable classes in the Jonah crab, the VD (for "ventricular dilator"). In this paper, we examine only passive properties of the VD cells, in the absence of voltage-dependent conductances, assessing the cell-to-cell variability in electrical properties and comparing it to the morphological variability. We have computed the contributions of different regions of VD to its electrotonic structure and have assessed the characteristics of passive electrical communication between different regions. We find that VD cells have a significant potential for heterogeneity in local computation. Brief reports of parts of this work have appeared previously (Hartline et al 1996; Hartline et al 1999).

The VD neuron occupies an interesting position in STG pattern generation. Its firing patterns vary more than those of most STG neurons under different conditions. It controls a muscle associated with the passageway between two compartments of the stomach (cardiac and pyloric), which helps explain its involvement in motor patterns of both regions (Russell 1977; Hooper and Moulins 1987). It must thus perform a variety of computational functions depending on conditions. Background against which such functions might be assessed is developed in our studies.

METHODS

Details of the methods for animal procurement and maintenance and for dissection, recording, identifying, filling and imaging crustacean stomatogastric ganglion (STG) neurons are given in Wilensky et al (2003) (see also Graubard and Wilensky 1994; Baldwin and Graubard 1995). Briefly, six cells of a single reidentifiable type, VD, from the STG of the Jonah crab, *Cancer borealis*, were injected ionophoretically with Lucifer Yellow CH or Texas Red lycinated dextran, fixed in paraformaldehyde, dehydrated and examined with a Biorad MRC600 laser scanning confocal microscope. Optical serial-sections were taken at 2 μm intervals, with a resolution of 0.665

– 0.75 μm/pixel. Stacks of serial sections were used to reconstruct cells quantitatively in 3D using NIH Image (by Wayne Rasband; URL: rsb.info.nih.gov/nih-image) image-analysis software. These six cells represent a subset of those presented by Wilensky et al. (2003). Macros written for NIH Image (available at www.pbrc.hawaii.edu/~danh/Resources/treetracedoc.html) allowed a circular profile to be centered in a process and the diameter adjusted to equal that of the process. Touching a key entered the location and diameter of the point digitized in a data structure along with information on the where the process connected to the tree. Branch points could be indicated, and a macro allowed automatic location of skipped branches to be digitized once any one path had been followed as far as possible. Neurites were followed to diameters of 1 pixel (ca. 0.7 μm), with an optical density of 100 or more on a scale of 255 (gain settings, fill intensity and other factors thus affected the completeness of tracings). Following digitizations, projections based on the data obtained were superimposed on the confocal projections to locate and include any neurites omitted from the original digitization. Data on neurite diameters, lengths and connectivities were used to generate input parameter files for the NEURON simulation software (Hines 1993, Hines and Carnevale 1997; www.neuron.yale.edu/neuron/). Version 4.2 was used for most studies, but 4.0 and earlier were also used. Each digitized neurite segment became a cylindrical "section" within the neuron model, composed of a single compartment (nseg=1). In this paper, we use the term "axon" to refer to the region of primary trunk distal to the last (most distal) secondary branch on each side. Because the axons extended well outside of the single microscope fields used for this work, the models were given extensions to each axon equivalent to 3 length-constants of additional cylinder of the same diameter as the last portion within the confocal image, divided into 200 compartments (nseg=200). Passive electrical parameters were taken from general measurements on STG cells rather than individual cases: R_m=50,000 Ωcm^2; R_i=60Ωcm. Somata of STG neurons are "infolded," i.e. the ratio of capacitance to surface area calculated on a spherical model and referred to a lipid bilayer is around 4 in *Panulirus* (Hartline et al 1993). In the absence of specific numbers for *C. borealis*, the

same value for infolding ratio was applied to the model cells used in this paper. Responses were computed to step or sinusoidal currents injected at various points in the cells. Distal (terminating) tips were assumed to be electrically sealed. Attenuation and transfer-impedance "dendrograms" were generated using the "electrotonic transform" capabilities of NEURON (Carnevale et al. 1995). In this paper, attenuations are expressed as effective electrotonic lengths, an e-fold attenuation corresponding to a unit electrotonic length. Data were analyzed using Kaleidagraph (Ablebeck Software) for statistics and curve-fitting.

Intrinsic errors

The methodology contains intrinsic sources of error that must be understood in order that limits on the validity of the results be appreciated. First, there is an unknown shrinkage of the tissue, estimated to be no more than 10% for cell bodies by sequential measurement of uninjected, injected, and fixed, whole-mounted tissue. Second, there are errors in measurement of the confocal images, especially in diameters. For thick processes, diameters were measured in the optical section presenting the greatest width of the profile at the measurement point. It is a matter of judgement where the boundary of such a process is, although usually it was sharp and errors of more than 1 – 2 pixels seemed unlikely. The situation in fine neurites was more ambiguous, and as the process diameter decreased toward 1 pixel, the likelihood of making errors increased. Further, with a limit of resolution of 1 pixel (0.635 – 0.75 μm), an error of 1 pixel becomes increasingly serious. To assess the magnitude of impact of this error, a test was run in which a uniform change in neurite diameter of 1 pixel was applied throughout a cell. This resulted in changes of 20-35% in computed DC input impedance at the soma, which gives an estimate for the order of uncertainty in quantitative measures presented here.

RESULTS

The VD motorneuron is a monopolar cell with a primary process that bifurcates within the ganglionic neuropil, extensions of the two subprimary processes becoming axons that run in the bilaterally-paired medial ventricular nerves to innervate a muscle on the ventral aspect of the stomach. The cell gives off a series of "secondary neurites" that ramify extensively in the ganglionic neuropil, receiving synaptic input from and placing synaptic output onto other processes in the neuropil. Figure 1A-F show reconstructed projections of all 6 cells in this study. The letters designating each panel are used in this paper to identify particular cells. Projections of the confocal stack in NIH Image, at two angles 10° apart, is shown as a stereo pair for one of the cells (VD_C) in Figure 1G. Details concerning neurite morphology of the VD cell type have been published in several papers (Wilensky, et al. 2003; Graubard and Wilensky 1994; Baldwin and Graubard 1995).

CELLULAR INPUT CHARACTERISTICS

The input characteristics of different morphological regions of the cell describe the voltage response at a point in the cell to current injected at the same point. They are important for assessing how a local region responds electrically to an imposed current such as generated by a spike or PSC. They also determine how that region reacts to artificial perturbations and what information this can yield above the cell. Three different approaches to portraying these characteristics are employed: examining the voltage responses to current steps, examining steady-state amplitudes as functions of frequency of an imposed sinusoidal current (Bode plot) and as a "dendrogram" representing the amplitude of sine-wave response as a function of position in the neuritic tree. The second aspect will be the characteristics of communication between regions. An understanding of these allows predictions to be made on how well signals, including spikes, PSP's and artificially-imposed perturbations, spread from a site of origin to other functionally important regions. They offer insight into the potential for computational heterogeneity in a neuron.

CELLULAR INPUT CHARACTERISTICS AT THE SOMA

Figure 2 presents membrane potential responses of the model cells to current injection at three different regions: 1) the soma; 2) the axon at its point of origin (most distal secondary branch point), and 3) the neuropil, including the regions of higher-order branching of neuritis out to the extreme ends at the distal tips. The left column of panels (Figs 2A, C, E) shows membrane potential trajectories at the injection site as a function of time following onset of a constant-current depolarizing step of 1 nA. The right column of panels (Figs. 2B, C, D) shows the amplitude of the voltage response at the same points to a sinusoidal current of amplitude ±1 nA, plotted as a function of frequency. The panels are discussed separately below, but they are presented together in a single figure to facilitate comparisons among the different regions.

Current steps to soma. Figure 2A shows simulations of 1 nA current steps in somata of each of the six reconstructed VD cells of this study. The different components of the complex charging curves come from different regions of the cell. The components can be identified by manipulating the model. As shown by Rall (e.g. 1969), the exponential trajectory at long time, represents the charging of the whole cell after shorter time-constant components have decayed. Charging occurs with nearly the membrane time constant, τ_0, equal to the product of specific membrane resistivity and capacitivity (set to 50 msec in all VD cell models). In the soma, this time constant dominates the overall charging trajectory. The faster components, which are significant for $t < \tau_0$ (Fig. 3A), represent the initial charging of the soma and the various neurite trees, as well as the equalizing time-constants along the infinite axonal cables. For VD cells, these amount to about 30% of the amplitude of the charging curve (Fig. 3A "τ_0 component"). The influence on the charging curve of different regions is illustrated in Figure 3A by first removing the axons (broken line) and then the neurites (dashes). The whole-cell trajectory follows first the isolated-soma charging curve, then

breaks away to follow the trajectory for soma plus neurites, and finally separates along its own trajectory as the axons begin to charge (Fig. 3A inset).

Bode plots. Voltage responsiveness to sinusoidal current of different frequencies gives an indication of how a cell will respond to rapidly vs slowly varying signals. Amplitudes for low frequencies predict response characteristics to slowly-changing currents; those to high frequencies are predictors for transient current responses. Analysis of sinusoids provides a basis for quantitative comparison among cell regions, as well as being helpful in formulating simplified models of a cell that retain its significant passive electrical features. The panels in the right hand column of the pairs in Figure 2 characterizing input properties at various points are "Bode plots" of the amplitude of response to sinusoidal current as a function of frequency. Figure 2B shows the Bode plots for current injected in the soma. The modeling data are presented as ratios of voltage response amplitude to amplitude of impressed current, i.e. the input impedance, Z_{in}. Bode plots are closely similar for the six VD cells, perhaps surprisingly so considering the variability in cell morphology. The initial constancy of impedance at low frequencies leads to a break at a "corner" frequency near 3 Hz. The corner frequency is determined by the membrane time constant ($f_c \sim 1/2\pi\tau_0$). The constant-amplitude region is followed by a more-or-less linear roll-off at high frequencies (see Table 2 for quantitative values), typical of behavior expected of various configurations of RC (resistance-capacitance) networks. A small but significant flare in the slope occurs around 50 Hz ("f_{break}" seen better in Fig 3B). To help understand the features of this passive AC characteristic of the VD, the normalized Bode plots of several simplified representations of a neuron are presented in Figure 3B. The isolated "soma" (simple parallel RC), at one extreme, has the same corner frequency as does the VD but a steeper roll-off (-1.0). The infinite cylinder, at the other extreme, rolls off with a gentler slope of –0.5. When the morphology of a monopolar neuron is represented as a spherical soma attached to an infinite uniform cylinder, the Bode plot is a better approximation to that of the VD

neurons in the low-frequency range (up to 50 Hz: Fig 3B broken line). The flare-out of the curve at high frequencies can be obtained by adding a short sealed cylinder of electrotonic 0.2λ, corresponding to the neuritic arborization, to the last-mentioned model (Fig 3B dashed line).

Regional contributions to the AC input characteristics at the soma site can be assessed using the same approach as for current steps, applied to the soma input admittance ($Y_{in} \equiv 1/Z_{in}$). Figure 3C plots the admittance normalized to that of the whole cell (solid line at ordinate 1.0) as a function of frequency with successive removal of the two axons (broken line), then all secondary branches (alternating long and short dashes), and finally the primary neurites (dashed line). All components except the primary neurites are major contributors to admittance at low frequencies and thus cannot be ignored in an assessment of load factors in VD cells. At higher frequencies, however, the relative contribution from axons diminishes rapidly with frequency, becoming negligible above 50 Hz. The contribution from the neurites increases and then decreases. Finally, as expected of electrically-extended cable-like structures, high frequencies are dominated by the near-by soma.

SPREAD OF SIGNALS FROM SOMA

Neuropil charging trajectories. In examining the spread of signals between different points of a neuron, it is well understood that voltage signals spread better from more central regions toward the periphery (e.g. soma to fine tips of neurites) than in the opposite direction (Rall and Rinzel 1973; Graubard 1975; Graubard and Calvin 1979, Carnevale et al 1995). As expected, this holds true for voltages produced by injection of current in VD somata and recorded in neurites out to the distal tips (Fig 4A). The time-course of tip charging for a typical VD is shown in Figure 4B. After charging is complete, tips achieve 90-95% of soma voltage levels. The principal difference distant neurite trajectories show compared to the soma record is their delay in the initial rise of around 1 msec at the start of the axon and up to 2 msec in distal tips (Fig 4B inset). Thus outward-spreading voltage control is extremely good in STG neurons at rest. However, while doubling the leak conductance

had only minor effects on attenuation at the tips, a 10-fold increase in leak resulted in over 50% attenuation at some tips.

Attenuation dendrograms. Attenuation characteristics of an entire arbor from a point within it can be depicted using a "dendrogram" of the electrotonic transfer function of the arbor (Carnevale et al. 1995). This plots the attenuation of the voltage, expressed as an equivalent "electrotonic distance" (the negative natural log of the relative signal strength) from any injection site in the tree to each other point, against the physical distance between the points. Figure 4C shows such a diagram for attenuation of DC signals from the soma to other parts of a VD cell. It is apparent that there is a steady attenuation along the twin primary trunks (representing the primary neurites and their axonal extensions). For the proximal region of these primary trunks, electrotonic distance increases at a rate corresponding to an electrotonic length-constant (the physical distance for an e-fold decrease in signal) of 2 – 3 mm. In the branched regions the increase is more gradual (λ~8mm). The latter situation is the result of a combination of a larger-diameter primary neurite working against the added losses derived from loading by the secondary branches. The increased diameter dominates over the loading by secondaries. Once into the secondary branches, however, attenuation with distance from the soma is greatly reduced. Secondary and higher-order neurites are almost isopotential, especially for DC signals. This seems anomalous at first, since the finer neurites, having higher axial resistance, might be thought to attenuate signals more rapidly than thicker processes. However, since the tips of all of the highest-order branches are sealed, escape of axial current is prevented. This produces "reflections" of the electrical signal, resulting in significantly less loss (Fig. 4C inset). Such is not the case for the primary neurites, for which the near-infinite axon provides a substantial current sink and hence the steeper voltage gradient. Still, for DC voltages, the overall attenuation from soma to any other point within the confines of the ganglionic neuropil is

quite small (8% in Fig. 4C). Attenuation increases with frequency for sinusoids, as will be described for axonal input sites.

CELLULAR INPUT CHARACTERISTICS AT THE AXON

Unlike many vertebrate neurons, generation and regulation of spike trains in STG neurons depend on current arriving at sites located several hundred microns from the soma along the primary trunks. Observed from the site of origin of each axon (the most distal branch point on the primary trunk), the electrotonic structure of the VD is somewhat different from that at the soma. The second pair of input curves of Figure 2 (Fig. 2C, D) illustrates this. Current steps applied to the axon elicit responses still dominated by the whole-cell time-constant, τ_0, hence qualitatively resembling that of the soma. However, here the initial rapid-rise component is emphasized (Fig. 2C) owing to the relatively larger input impedance at high frequencies present at non-somatic sites. A substantial amount of variability among cells is revealed in the magnitude of this rapid phase (Fig 2C inset). The Bode plots for current injection at the axon origin also reflects the more cable-dominated behavior (Fig. 2B). While similar to that for the soma at the lower frequencies (Fig. 2D), the roll-off is not as steep. This results in elevated input impedances at high frequencies that enhance the rapid component of charging seen in the step responses. The variability in the early transient phase of the current-injection graphs is reflected as variability in the high-frequency end of the Bode plots, relative magnitude of the transient showing a good positive correlation with input impedance at high (100 Hz) frequency at the axonal site.

SPREAD OF SIGNALS FROM AXONS

Attenuation dendrograms. Figure 5 shows attenuation dendrograms computed for the origin of one of the axons (most distal secondary branch point) of a VD. At DC (Fig. 5A), electrotonic distance (attenuation) increases relatively rapidly along the primary axes of the cell, from the origin

out along the axon on the one hand, and at roughly equal rates back along the primary neurite of the same side and out along the opposite primary neurite. Attenuation along subsidiary neurites, as was the case for the somatic point of reference, is minimal. What shows more clearly in this dendrogram is the strong gradient of attenuation to different regions of synaptic input and output in the neuropil. There is little attenuation to neurite tips derived from secondaries branching from the primary trunk near the origin of an axon (triangle symbol, Fig. 5A). The most distal secondary of the opposite side, however, shows several times this attenuation (square symbol, Fig. 5A), and the tips of neurites between show a spread of values depending on their location relative to the current-injection site. This situation suggests that the potential for synaptic output generated by voltage perturbations near the axon origin could vary substantially as a function of distance from the site. The absolute range of attenuation at DC (and hence for slow signals) is minimal from axonal sites (mean of 19±9%; Fig. 5A), but for signals with frequency components above the corner frequency, this situation changes. Dendrograms for this same cell at frequencies of 0, 75 and 250 Hz are shown superimposed in Figure 5B. At frequencies corresponding approximately to the width of a spike (250 Hz), attenuation to nearby tips is still low, while that to distant tips reaches orders of 95% (Table 2). This gives a quantitative estimate for the electrotonic extent of each cell from an axonal reference point.

Attenuation properties for axonal signals are quantitatively dependent on the current sinks provided by the soma and, in VD cells, the contralateral axon. For VD_C, for example, removal of the entire contralateral side reduces by 1/3 the electrotonic distance from the axon origin to the soma. The reduction decreases to only 11% at 250 Hz owing to the increase in load from nearby regions. Reduction in electrotonic distances to nearer regions of the cell are smaller. The impact of the soma is even greater. Its removal drops the electrotonic distance from the axon origin to the junction of the primary neurite with the soma by over half (55%) at 0 Hz and almost 40% at 250 Hz.

CELLULAR INPUT CHARACTERISTICS IN NEUROPIL

The last pair of input characteristics of Figure 2 (Fig. 2E, F) present data for injection and recording sites colocalized at different points along a secondary trunk of VD_C, extending out to a distal tip. Electrode locations are shown in Figure 6A.

Current injection. Responses to long current pulses are shown in Figure 2E. As the injection site is moved distally along the trunk, there is a progressive increase in the magnitude of the voltage response owing to a progressively increasing input impedance as the process gets smaller and more distant from central loading regions. There is also a trend of increasing relative magnitude of the initial fast-rise component of the trajectory: at proximal sites in the secondary tree the slow component dominates. At a point around half way to the farthest distal tips (between the sites labeled 810 and 844 in Fig. 6A), the rapid component surpasses the slow, and continues to grow with more distal siting while the slow component changes little. This change in dominance of the rapid component shows up especially well in plots normalized to the asymptotic level (Fig. 6B). At the tips, the rapid component reaches an extreme, dwarfing by several fold the slower, delayed rise governed by membrane time constant. The reason for the rapid rise is that the initial charging is governed by the low access resistance between the current source and near-by uncharged regions of the cell. Charging slows down rapidly as neighboring capacitances charge up and more distant regions with higher access resistances begin to charge. After a few milliseconds, only the slow charging of the whole cell (soma, primary processes and other secondary trees) is left. The rapid response is potentially quite significant for the local computation properties within the neuropil. Synaptic conductance changes in the distal regions will have an immediate effect on local membrane voltage, and hence be capable of rapid impact on nearby synaptic output sites. Filtering through the membrane time constant, which gives rise for example to typical long rise times in PSPs recorded from cell bodies, will only be significant for sites distant from the input (in fact beyond the reaches

of the same secondary arborization). Were a synapse to occur on the soma (which does not happen in STG) this phenomenon would be absent, and PSPs would be slow-rise throughout the tree. This dichotomy in synapse kinetics may be part of the explanation for the almost ubiquitous dendritic design in nerve cell morphology, instead of more compact designs.

Bode plots. Plots of input impedance vs frequency along the secondary neurites and extending out to the tips are shown in Figure 2F. They present a progressive further deviation from the characteristics of a ball-and-stick model computed for a soma electrode. Starting at proximal sites near the primary process (Fig 2F "740"), plots resemble those for the axon origins shown in Figure 2D. Proceeding distally, they show a progressive increase in DC input impedance as neurite diameter decreases. In the VD cell type, at least, there is not enough additional membrane being added by the branching of neurites to compensate for the diameter decrease. At sinusoidal frequencies just above the corner frequency, the roll-off in the Bode plots is less steep than for the soma and decreases with distance along the neurite. It reaches that of an infinite cable about half way out to the farthest distal tip (Fig 2F "810"). Between ca 10 and 100 Hz, a flattened region develops in the plot for more distal neurites. Roll-off resumes above a few hundred Hz. The impedance in the flattened regions rises more rapidly than the DC impedance as more distal sites are examined until near the tips, impedance is nearly flat at all frequencies up to several hundred Hz. The behavior near the tips resembles that of a flared cable (see example plotted in Fig. 3B), which indeed the morphology of expanding surface over several hundred microns in the proximal direction qualitatively resembles. This nearly flat frequency response of the most distal neurites (e.g. Fig. 2F 855; 862) underscores the observation that membrane voltage in the fine processes can follow rapid temporal patterns of input current very precisely.

Impedance dendrograms. Input impedance of the fine neurites is difficult to compute accurately in our material owing to the poor spatial resolution for our images of the fine processes. Thus Figure 6B shows an input impedance dendrogram giving an approximation of the impedance at each point in the cell as a function of its physical distance from the soma. The parallel trajectories for the fine neurites are artifacts of the pixel-derived quantization of process diameter. The apparent linearity of the trajectories is only approximate, but is a property of the spatial-dependence of the impedance of an electrotonically short cylinder with one end sealed and the other open. Although the absolute error in impedance values is substantial for the fine neurites, the plot makes clear that it is high at the tips, decreasing rapidly with approach to the more central trunk. This pattern is expected, and has been reported previously in several other cell types (e.g. Graubard 1975; Graubard and Calvin 1979; Buchannan et al., 1992; Jaffe and Carnevale 1999)

SPREAD OF SIGNALS FROM TIPS

With current applied at one of the tips, voltage is typically attenuated in excess of 80% in spreading back to the soma and into tips derived from other secondary branches. This is illustrated in Figure 7A which shows the voltage responses at two sets of neurite tips for the examplar cell, VD_C. One set of well-separated traces derives from branches off of the same secondary trunk as the injection site (see placement diagram at right). Tips branching from different secondaries produce the overlapping traces condensed at the bottom and shown on an expanded scale in the inset. Only tips branching off near the injection site retain a modest level of coupling. Note that there is a slight disparity in responses of the tips depending on whether they derive from ipse- or contralateral trunks. Similar results were obtained by Glasser (1977) and by Graubard and Calvin (1979) in other STG neurons. This asymmetry in voltage attenuation is owed to the large disparity in input impedance at the two points: a large current is needed to alter voltages in the central regions of a cell by a given amount, and this current spreads well in polarizing distant regions. A much smaller current suffices

to alter the voltage in a small-diameter (large input impedance) process, and the current is rapidly dissipated by the electrical load of the rest of the cell.

Dendrograms. Figures 7B and C show attenuation dendrograms for DC and 100 Hz, respectively, from neurites and other points in the cell to the axon origin, the gateway to the spike trigger zone. Here, current injected into the fine processes is sunk into the expanding surface of more proximal neurite branches as well as the heavy loads of soma and axons, producing the steep attenuation. These dendrograms are the "conjugates" (opposite direction) for those shown in Figure 5. Note that even the electrotonic distances along the axons toward the axon origins are shorter than in the reverse direction (λ~700 μm).

Transfer impedance. Heretofore, we have focused on the attenuation of *voltage* along the branching structure of the neuron. A somewhat different view is obtained by examining the effects of injecting a fixed amount of *current*, as might result from a small synaptic event, at different points in the neuritic tree. The voltage response evoked by such a current is directly proportional to the input impedance at a site. As Graubard and Calvin (1979) demonstrated, this means that moving the site of current injection to various points on a cell has much less impact on the voltage response at a fixed reference point than moving a voltage source around, a property referred to as "passive normalization" by Jaffe and Carnevale (1999). The concept of "transfer impedance" applied to neurons formalizes this. The transfer impedance to a recording site, r, from a source site, s, is given by:

$$Z_{r,s} = V_{r,s} / i_s$$

where $V_{r,s}$ is the voltage response at the recording site due to i_s the current injected at the source site. Note that the attenuation factor, α_{rs} (the fraction of voltage signal remaining at the recording point), is simply $Z_{r,s}/Z_{in,s}$. The reciprocity theorem of passive electrical circuit theory (e.g. Brenner and Javid, 1959) states that $Z_{a,b} = Z_{b,a}$, in other words, with a current injected at the axon origin and a recording electrode in a dendrite tip, the same voltage response, in both magnitude and time-course, will be observed as if that same current is injected at the tip and the recording is made from the axon.

Thus the transfer impedance gives a direction-independent measure of communication between two parts of a cell. Figure 8A shows transfer-impedance dendrograms for a reference site at one of the axon origins of VD_C at four different frequencies. A salient feature of this figure is the strong decrease of $Z_{r,s}$ with frequency for the whole tree (since $Z_{r,s} = \alpha_{rs} Z_{in,s}$, and both attenuation factors and input impedances decrease with frequency, this makes sense). Even over a modest frequency range (0 – 5 Hz) transfer impedance is affected more than it is by spatial location within the neuritic tree. Spatially, the transfer impedance from the axon origin to other parts of the cell still exhibits a strong gradient along the primary trunk of the cell, with little variation along secondary and higher ("off-axis") neurites. As was the case for the attenuation dendrogram, the gradient of the transfer impedance dendrogram is steeper for secondary neurites arising from the ipselateral primary neurite.

In working with transfer impedances, it is sometimes convenient to use a "current effectiveness," $\varepsilon_{r,s}$, generated by normalizing the transfer impedance to the input impedance at the site of interest (e.g. the axon origin):

$$\varepsilon_{r,s} \equiv Z_{r,s}/Z_{r,r}$$

A value of $\varepsilon_{r,r} = 1.0$ is then the reference value for a current injected at the site of interest (since $Z_{r,r} = Z_{in,r}$ at the recording site) and $\varepsilon_{r,s}$ is the ratio of voltage responses at other sites to that at the reference site ($Z_{r,s}/Z_{r,r} = V_{r,s}/V_{r,r}$). For current injected at sites, s, having values of $\varepsilon_{r,s}$ close to 1.0, there is at the reference site, r, very little difference in voltage response compared to that from the same current at the reference site. Figure 8B shows the data from Figure 8A expressed as current-effectiveness. The dendrogram for $\varepsilon_{axon,s}$ at DC is squeezed at the top of the diagram, all values being near 1.0. For all VD cells taken together, its extreme values between the axon origins and the farthest distal tips ranged between 0.7 and 0.9 . In other words, for a sustained current, there is predicted to be no more than a 30% decrement in voltage response at the trigger zone regardless of where the current is injected. A similar result was found by Graubard and Calvin (1979) for another STG neuron type, the AM. This passive normalization holds well for low frequencies (e.g. to 10 Hz) but breaks down as frequency increases (Fig. 8B). Use of the $\varepsilon_{axon,s}$ representation removes that part of the frequency-dependence of $Z_{axon,s}$ that results from the input impedance, but it leaves the dependence on α_{rs}.

Transfer impedance declines with frequency in parallel with input impedance. The range to the extreme non-axonal parts of a cell is greater at higher frequencies. ε_{min} ~ 0.1 to 0.3 for the different VDs at 100 Hz, a frequency that approximates those found in PSP's. Differences in transfer impedance between two parts of a cell remain relatively independent of frequency (ca 3 - 4 MΩ between extremes; Fig. 8B).

It is evident from inspection of attenuation and transfer-impedance dendrograms that values taken from different locations tend to cluster in groups corresponding to the different secondaries. This grouping can be seen more quantitatively in histograms of the parameters for the neurite tips in a tree. Figure 8C and D show such histograms, at 0 and 100 Hz respectively, for transfer impedance

with respect to the left axon origin in VD_B. The groupings of this communication parameter are clear. The groupings are relatively more segregated at higher frequencies on the ipselateral side owing to the greater attenuation rates along the primary trunk. Thus, there seems to be no continuum in the communication-characteristic spectrum, opening the possibility that each secondary with its own role to play in cellular integration may have its own communication parameters with other parts of the same cell.

DISCUSSION

The calculation of response properties and inter-regional communication in a single stomatogastric cell type has yielded several intriguing insights into how even the passive properties of stomatogastric neurons may figure importantly in neuronal information processing in the ganglion. The background for understanding much of this is provided by Graubard and Calvin (1979), which source may be consulted for a more detailed discussion:

Input characteristics of VD cells. The frequency-dependence of the input impedance at the soma of VD neurons fits reasonably well with a ball-and-stick model, the "stick" being an infinite cable. The fit is best for equal DC impedances for the sphere and cable. This fits well with the monopolar morphology of stomatogastric motorneurons. Better fits at high frequencies are obtained by adding a short terminated cable of electrotonic length 0.2 in parallel with the infinite cable, dividing the DC conductance equally between them. Soma, neurites and axons all contribute significantly to input impedance measured in the soma at low frequencies. High frequencies are soma-dominated (as expected). The soma of a stomatogastric neuron does not support regenerative events, although it possesses several voltage-dependent conductances (Graubard and Hartline 1991). Its passive electrical properties give it importance in loading events that occur in other parts of the cell. Its active properties suggest that its impact will increase as greater depolarizations are reached.

The attenuation of somatic signals will thus have some impact on the computational properties of the cell. Input impedances rise as neurite diameter decreases. AC characteristics at more peripheral locations show reduced attenuations at high frequencies owing to loading by more central membrane.

Peripheral spread of signals. The passive electrical properties of VD cell neurite trees follow basic patterns long recognized for other similarly-branched cable structures. Even though there are essential active properties to be taken account of in later studies, these passive properties provide the framework for understanding computational characteristics of VD cells (see Segev and London 1999). Included are those summarized by Segev and London as the "seven insights:" The profile of voltage spread from a current-injection site is highly asymmetrical, being severely attenuated going centrally from a distal site of origin and much less so in the opposite direction. On the other hand, voltage-response amplitude measured at a fixed point to a given current injected at some other site is less dependent on site location (see also Graubard and Calvin 1979; Spruston et al 1999). Thus, for slow events, communication from the primary trunk of a VD cell to its distal neurites is strong. In a "resting" state, with only low-conductance subthreshold events active, the cell is predicted to be almost isopotential. This prediction rests on the currently untested assumption of uniformity of passive properties, deviation from which could cause significant revisions in expected distribution (e.g. Segev and London 1999). However, VD cells also show distinctive properties that relate to their particular morphologies. Perhaps the most interesting is that for rapid events, the magnitude of perturbation in a neurite due to events in another part of the tree (such as the axon) becomes significantly dependent on the position of the branch point of the secondary tree from which the neurite under consideration descends. Thus neurites descended from secondaries arising distally along the primary trunk appear suited for spike-mediated synaptic transmission; those descended from more proximal secondaries for non-spiking transmission.

Impact of bilateral symmetry in VD. The VD cell is predicted to possess some unusual electrical characteristics by virtue of its having two relatively large axons branching proximal to the origins of many of the secondary neurites. Unlike a fully monopolar cell, having a single primary trunk, the trunk on one side of the VD loads signals occurring on the other side. For example, in a fully monopolar neuron the voltage produced in the axon and reaching the branch point of a secondary neurite would not be much more attenuated in reaching the soma but in the VD, there is a significant further attenuation owing to the second subprimary process.

Regional isolation. Computation of signal attenuation characteristics has shown that the tips of different secondary trees, even with the high-resistance (and hence large length-constants) of passive membrane, are potentially well-isolated electrically from each other, hence:

a. They may integrate input independently. They could potentially initiate active responses, such as plateaus, independently.

b. They may be capable of local computation. Each major secondary or tertiary branch is potentially a separate functional unit.

c. By themselves, they have relatively weak influence on the trigger zones. This is consistent with a dependence on plateau mechanisms to carry excitation to the trigger zones. It is also consistent with the control of plateaus by weak inputs.

d. Although individually relatively weak in trigger zone influence, the magnitude of influence of individual synapses varies only moderately with location. Thus for passively spread synaptic events, at least, the cell is free to adjust synapse placement to optimize other factors. From this perspective it seems a minor concern that the soma and more proximal neurite regions of STG neurons are tightly wrapped in glia and support no synapses (King 1976).

Local vs global computation. "Local computation," the regulation of synaptic output at sites physically close to sites of synaptic input, is, for a given input site, stronger for outputs located at or distal to the site than for those proximal. This is a point raised earlier by Graubard and Calvin 1979). On the other hand, "global computation" is favored by more proximal inputs; this appears to be limited in STG neurons. Additional mechanisms may favor global computation. These mechanisms include regenerative events in neurites and the distribution of single synaptic inputs over several neurites. On the other hand, active membrane mechanisms that load the primary trunk, such as repetitively spiking axons or active outward currents may tend to isolate different secondaries from each other even more.

Comparison with intradendritic communication in other cell types. Other studies have focused on issues of passive intracellular communication among regions for a variety of neuron types in various systems, especially in vertebrate brain (see e.g. reviews in Stuart et al 1999). Jaffe and Carnevale (1999) present analyses of the passive communication properties within 5 classes of vertebrate CNS neurons (CA1 and CA3 pyramidal, CA3 non-pyramidal, layer V PFC pyramidal and dentate gyrus granule cell). Their results showed several of the same features as those for VD cells, and some differences. The relative constancy of transfer impedance to central regions from side branches off basal dendrites of CA1 cells mirrored the effects seen in VD secondary trees for similar reasons (sealed ends). Jaffe and Carnevale (1999) suggest this feature could afford side branches sufficient surface area to support multiple converging inputs while giving them equal access to more central regions of influence. The location-independence of transfer impedance to the soma (z^ for Jaffe and Carnevale 1999; $Z_{soma,s}$ for the present paper) at low frequencies (20 Hz) for CA3 pyramidal cells mirrored that to all points along the primary neurite (including soma) seen in VD cells (Fig. 8B). The graduation of transfer impedance along the cell axis (primary trunk) seen only at high frequencies (100 Hz) in VD (Fig. 8D) is prominent at low frequencies (20 Hz) along the

apical dendrite of CA1 and layer V pyramidal cells (but not for CA3 cells). In this respect VD resembles CA3 pyramidal and non-pyramidal neurons more closely than CA1 in passive properties. Possession of a large primary dendrite appears to figure centrally in producing location-dependent transfer impedances in mammalian cells. The primary neurite of STG neurons might play a similar role, but it would appear that this is limited to high frequencies.

ACKNOWLEDGEMENTS

We thank Drs. Michael Hines and Ted Carnevale for making NEURON simulation software available to us and helping us repeatedly in familiarization with its operation and uses. We thank Leanna Bartram, Anna Cooke, Amy Hower and Steve Lum for assistance reconstructing cells and making modeling runs.

LITERATURE CITED

Baldwin DH, Graubard K. 1995. Distribution of fine neurites of stomatogastric neurons of the crab *Cancer borealis*: Evidence for a structured neuropil. J Comp Neurol 356:355-367.

Brenner E, Javid M. 1959. Analysis of Electric Circuits New York: McGraw-Hill.

Buchannan JT, Moore LE, Hill R, Wallen P, Grillner S. 1992. Synaptic potentials and transfer functions of lamprey spinal neurons. Biol Cybern 67:123-131

Bullock TH, Horridge GA. 1964. Structure and Function in the Nervous System of Invertebrates. San Francisco: W.H. Freeman.

Carnevale NT, Tsai KY, Claiborne BJ, Brown TH 1995. The electrotonic transform: a tool for relating neuronal form to function. In Tesauro G, Touretzky DS, Leen TK, editors: Advances in Neural Information Processing Systems Vol. 7. Cambridge, MA: MIT Press. p 69-76.

Glasser SM. 1977. Computer Reconstruction and Analysis of Motor Neurons in the Lobster Stomatogastric Ganglion. Ph.D. Thesis, University of California, San Diego (Physics).

Graubard K. 1975. Voltage attenuation within *Aplysia* neurons: the effect of branching pattern. Brain Res 88: 325-332.

Graubard K, Calvin WH. 1979. Presynaptic dendrites: Implications of spikeless synaptic transmission and dendritic geometry. In Schmitt FO, Worden FG, editors: The Neurosciences Fourth Study Program. Cambridge, MA: MIT Press. p 515-524.

Graubard K, Hartline DK. 1991. Voltage clamp analysis of intact stomatogastric neurons. Brain Res 557:241-254.

Graubard K, Wilensky AE. 1994. Morphology of stomatogastric neurons of *Cancer borealis*. Soc. Neurosci. Abstr 20:1414.

Hartline DK. 1967. Impulse identification and axon mapping of the nine neurons in the cardiac ganglion of the lobster *Homarus americanus.* J Exp Biol 47:327-340.

Hartline DK, Gassie DV, Jones BR. 1993. Effects of soma isolation on outward currents measured under voltage clamp in spiny lobster stomatogastric neurons. J Neurophysiol 69: 2056-2071.

Hartline DK, Graubard K, Bartram L, Wilensky AE. 1999 Electrotonic structure of reconstructed VD neurons of crab stomatogastric ganglion. Soc Neurosci Abstr 25:1646.

Hartline DK, Graubard K, Wilensky AE, Orr G 1996. Computation styles in identified neurons from the crab stomatogastric ganglion. Soc Neurosci Abstr 22:132.

Helmchen F. 1999 Dendrites as biochemical compartments. In Stuart G, Spruston N, Häusser M. editors: Dendrites. Oxford: Oxford University Press. p 161-192.

Hines ML. 1993. NEURON – a program for simulation of nerve equations. In Eeckman F, editor: Neural Systems: Analysis and Modeling. Norwell, MA: Kluwer. P 127-136.

Hines ML, Carnevale NT. 1997. The NEURON simulation environment. Neural Computation 9: 1179-1209.

Hooper, SL, Moulins, M. 1987. Switching of a neuron from one network to another by sensory-induced changes in membrane properties. Science 244: 1587-1589

Jaffe DB, Carnevale NT 1999. Passive normalization of synaptic integration influenced by dendritic architecture. J Neurophysiol 82:3268-3285.

King DG. 1976. Organization of crustacean neuropil II. Distribution of synaptic contacts on identified motor neurons in lobster stomatogastric ganglion. J Neurocytol 5**:**239-266.

Maynard DM, Walton KD. 1975. Effects of maintained depolarization of presynaptic neurons on inhibitory transmission in lobster neuropile. J Comp Physiol 97:215-243.

Otani T, Bullock TH. 1959. Effects of presetting the membrane potential of the soma of spontaneous and integrating ganglion cells. Physiol Zool 32:104-114.

Rall W. 1962. Theory of physiological properties of dendrites. Annals N Y Acad Sci 96:1071-1092.

Rall W. 1964. Theoretical significance of dendritic trees in neuronal input-output relations. In Reiss RF, editor: Neural Theory and Modeling Stanford CA: Stanford University Press. p 73-97.

Rall W. 1969. Time constants and electrotonic length of membrane cylinders and neurons. Biophys J 9: 1483-1508.

Rall W, Shepherd GM, Reese TS, Brightman MW. 1966. Dendrodendritic synaptic pathway for inhibition in the olfactory bulb. Exp Neurol 14:44-56.

Rall W, Rinzel J. 1973. Branch input resistance and steady attenuation for input to one branch of a dendritic neuron model. Biophys J 13: 648-688.

Russell, D.F. 1977. *Central Control of Pattern Generators in the Stomatogastric Ganglion of the Lobster* Panulirus interruptus. PhD dissertation, Univ. Calif. San Diego, Biology.

Segev I, London M. 1999 A theoretical view of passive and active dendrites. In Stuart G, Spruston N, Häusser M, editors: Dendrites. Oxford: Oxford University Press. p 205-230.

Spruston N, Stuart G, Häusser M. 1999 Dendritic integration. In Stuart G, Spruston N, Häusser M, editors: Dendrites. Oxford: Oxford University Press. p 231-270.

Stuart G, Spruston N, Häusser M. 1999. Dendrites. Oxford: Oxford University Press.

Tauc L, Hughes GM. 1963. Modes of initiation and propagation of spikes in the branching axons of molluscan central neurons. J Gen Physiol 46:533-549.

Watanabe A. 1958. The interaction of electrical activity among neurons of lobster cardiac ganglion. Jap J Physiol 8:305-318

Wilensky AE, Baldwin DH, Christie AE, Graubard K. 2003. Stereotyped neuropil branching of an identified stomatogastric motor neuron. J Comp Neurol 466: 554-563

FIGURE LEGENDS

FIGURE 1. VD cells from the stomatogastric ganglion of a crab. A-F: Projections of 3D reconstructions of the 6 cells used in this study. Anterior direction up. Circular somata scaled to cell dimension have been superimposed on the projections. Letters in these panels are used to identify specific cells throughout the paper. G: Projections of the confocal microscope "stacks" of optical sections through cell VD_C presented as a stereo pair. Calibration bar: 50 μm. Arrow indicates anterior. These cells correspond to the following figures of Wilensky et al 2003: VD_B= Fig. 2A, 3A, 4; VD_C=Fig 2B, 3B; VD_D = Fig. 2C, 3C.

FIGURE 2. Input characteristics of VD cell regions.

A. Simulated response for each of the 6 VD neurons of this study to 1 nA of depolarizing current injected into soma. Line codes apply to panels A-D.

B. Bode plots for 6 VD cells, showing the amplitude of the voltage divided by the amplitude of impressed sinusoidal current as a function of frequency (log-log scale). Straight broken lines intersecting at the corner frequency (f_{corner}) show input impedance at 0 Hz (horizontal line; Z_{0Hz}) and roll-off slope (diagonal line) for one of the cells.

C. Input characteristics of axons. Voltage simulations for the points of origin (initial sections) of all 12 VD axons in response to a current step injected at the same point. Inset, first 5 ms of response (voltage scale –65 to –60 mV) showing variability in initial trajectory.

D. Bode plot (log-log) for VD axons. Note variability in high-frequency behavior.

E. Simulated response to 1 nA current injected and recorded at sites spaced *ca* 50 μm along one secondary neurite trunk (the 6th most distal secondary from the soma along the left trunk, designated "ℓ6") of VD_C. Trace numbering corresponds to sites labeled in Fig. 6A. Unnumbered traces (top to bottom): 744 and 740 respectively. Inset: expanded sweep: note very rapidly-rising (<1 msec) phase for distal points.

F. Bode plots for the same sites in the secondary neurite of E. Note retention of high gain at high frequencies.

FIGURE 3. Details of soma input characteristics.

A. Simulated response of a VD neuron (VD_B) to 1 nA of depolarizing current injected into the soma. Solid line: trajectory for whole cell. Long-short broken line "no axons" produced by removal of axons. Dashed line: "soma only" produced by removal of all neurites. Top of frame

represents asymptotic level for whole-cell trajectory; dotted line merging with whole-cell trajectory represents just the membrane time-constant component of charging (τ_0). Inset shows the initial 5 msec of the charging curve. B. Plots for simplified models approximating VD characteristics (see text). Broken line: sphere + infinite cylinder, the ratio of the DC input admittances 1:0.5 (sphere:cylinder) ; dashed line: sphere + infinite cylinder + 0.2λ cylinder with admittance ratio 2:1:1. Dotted lines: extremes represented by sphere, semi-infinite cylinder and flared cylinder. The latter expands in diameter from 1 to 500 μm over 10 cm, approximating the 10-fold expansion of a VD process from distal neurite to axon over ca 200 μm.

C. Normalized soma input admittance (=$1/Z_{in}$) vs frequency plot (linear) for VD_F showing effect of removing different regions of the cell. Normalized admittance for whole cell is defined as 1.0 at all frequencies (solid line). Broken line: removal of axons causes drop in admittance only at low frequencies. Dashed line: removal of secondary neurites. Dotted line: removal of primary neurites.

FIGURE 4. Electrotonic communication from soma to neurites.

A. Diagram of standard tip sites of exemplar cell VD_C. Each tip is from a different secondary and represents one of the longer paths through the secondary branch. lax = left axon origin; rax = right axon origin. Numbers serve as identifiers for electrode placements indicated in other figures. Unnumbered sites (left to right): 477, 1204 (below), 155, 1770, 737, 977, 1609. Site 643 overlies the left axonal origin.

B. Simulated voltage recordings from neurite tips indicated in the diagram of Panel A in response to a 150 msec-long step of current injected in the soma; normalized to the asymptotic level reached in soma. Communication between soma and neurites is directional. From the soma out, DC attenuation is small and mostly confined to primary neurites. Inset shows initial trajectories for the soma, both axon origins, and the two neurite tips from the standard set (Diagram in panel A) showing the most divergent trajectories (1609; 643). Note differences in delays.

C. "Dendrogram" of electrotonic distance from soma to all parts of examplar cell VD_B. (a unit electrotonic distance corresponds to an e-fold attenuation) for DC signals applied to soma ("gain" scale: fractional signal remaining). Plotted as a function of physical distance from the soma (abscissa). Length constant of 3.7 μm-diameter axon-extensions = 2.8 mm.

FIGURE 5. Electrotonic communication from axon origin to rest of cell.

A. DC attenuation dendrogram showing electrotonic distance of the different points in the cell as a function of physical distance from the origin of the right axon (Cell VD_B).

B. Attenuation dendrogram for 3 frequencies: 0, 75, 250 Hz from the same location. Inset: Electrotonic distance ("L") from the right axon origin as a function of frequency (log scale) for the soma (*) and two neurite tips, one from the left (contralateral) side (square symbol on main diagrams) and one from the ipselateral side (circle).

FIGURE 6 Input characteristics in neuropil.

A. Secondary tree "ℓ6" (6^{th} branch along left primary trunk) of exemplar cell VD_C. Standard electrode sites for recording along the secondary trunk indicated by circles and numerical ID's.

B. Normalized charging curves for current injected at locations indicated on diagram of Panel A and recorded from the same site. (VD_C). Note the increasing dominance of the fast initial phase at more distal sites.

C. Input impedance dendrogram for 0 Hz. Plot vs distance from soma. Parallel lines for the most distal neurites is an artifact of the pixel-based quantization of neurite diameter (multiples of 0.69 μm). (VD_B)

FIGURE 7. Electrotonic communication from neuropil to rest of cell.

A. Charging trajectories in response to a long 1 nA current pulse injected into a left-side tip (862). Colored (/grey) traces: recording sites are from selected distal neurite tips arising from different secondary branches (see site diagram, Panel A, Fig 4). Black traces: sites along the same secondary trunk (diagram above: arrow "i" indicates injection site; circles recording sites). Voltages along the secondary axis rise abruptly, then more slowly as the whole cell charges (*cf.* Fig. 2E). Note that the fall-off in voltage with distance from the injection site is steep at first and lessens as the neurite diameter increases. Initial rapid phase of charging is more pronounced at more distal sites. Voltages at tips arising from each of the 12 non-shared secondary neurites are much smaller and lack the rapid component, illustrating tip-to-tip isolation across secondaries. There are slight differences between left-side and right side origins of the secondaries (inset). $Z_{in,\ 0\ Hz,\ 862} = 201\ M\Omega$.

B., C. Attenuation dendrograms for VD_B from the various parts of the cell to the left axon ("conjugate" diagrams to parts of Fig. 4). 0 and 100 Hz respectively. Inset shows frequency-dependence (log scale) of attenuation between two tips, one from each side (circle: ispelateral; square symbol: contralateral) to the origin of the left axon.

FIGURE 8. Transfer characteristics between axonal origins and other sites in VD.

A. PSP's generated in VD_C by alpha synapse (see caption to Fig. 12). Solid line: recording at the left axonal origin of PSP produced by synapse placed at a secondary tip (862, diagram in Fig 10A). Broken line: recording at tip 862 of PSP produced by synapse placed at left axonal origin. The PSP's superimpose because of reciprocity in the transfer impedance. Dotted lines: recordings at sites of synaptic input ("(862)"=tip; "(ax)"= left axonal origin).

B. Impedance dendrograms at 0, 5, 10 and 100 Hz in VD_C (top to bottom) with respect to the right axon origin. Left scale": impedance magnitude (MΩ). Right scale: transfer impedance normalized to input impedance at axon origin for each frequency, representing "conductance efficacy:" the voltage response amplitude expected at the axon from a small sinusoidal conductance change at different points on the cell measured as a fraction of that produced by the conductance placed at the axon (see text).

C. Transfer-impedance histograms at 0 Hz (upper panel) and 100 Hz for left axon origin (401) for exemplar cell VD_B. Upper scale: impedance (MΩ); lower scale: "conductance effectiveness," ε_{axon}, relative to left axonal origin. Note histogram peaks corresponding to the different secondary trees (*cf* dendrograms above). Note that at the higher frequencies, secondary clusters are more segregated on the ipselateral side owing to steeper attenuation along the primary trunk (note change in vertical scale). Bin sizes: 0.05 MΩ at 0 Hz; 0.03MΩ at 100 Hz.

TABLE 1: Input characteristics

		VD_A	VD_B	VD_C	VD_D	VD_E	VD_F	Mean	SD	CV
SOMA										
$Z_{in,0.1}$ (MΩ)		31	28	28	34	35	31	31	3.0	10%
f_{corner}		3.0	3.3	3.1	3.0	3.2	3.0	3.1	0.13	4%
f_{break}		55	65	75	59	68	40	60	12.2	20%
Roll-off		-0.85	-0.89	-0.88	-0.82	-0.86	-0.90	-0.87	0.032	4%
$g_{whole\ cell}$		0.033	0.033	0.035	0.029	0.029	0.032	0.032	0.0024	8%
$g_{soma+prim+sec}$		0.023	0.025	0.027	0.024	0.019	0.025	0.024	0.0029	12%
$g_{soma+primaries}$		0.014	0.016	0.017	0.016	0.012	0.015	0.015	0.0018	12%
g_{soma}		0.012	0.013	0.014	0.014	0.010	0.013	0.013	0.0015	12%
ρ		1.8	1.5	1.5	1.1	1.9	1.5	1.5	0.28	18%
AXON ORIGIN										
$Z_{in,0.1}$	ℓ	39	30	30	42	41	32			
								34	4.7	13%
	r	35	29	31	40	37	33			

Input characteristics of 6 VD neurons at 0.1 Hz ("DC"). Z_{in}: input impedance amplitude; f_{corner}: corner frequency (Hz); f_{break}: frequency (Hz) of "break" in roll-off, where slope changes abruptly; Roll-off: slope of intermediate-frequency range (10-f_{break}) on log-log plot. g: input conductance ("admittance")(1/Z) for whole cell, for soma + primary neurites + secondary trees (i.e. cell less the axons), for soma + primary neurites, and for soma alone, as indicated by subscripts (μmho)(DC). $\rho = (g_{whole\ cell}-g_{soma})/g_{soma}$. Input impedance amplitude only is shown for origins of left (ℓ) and right (r) axons.

TABLE 2: Electrotonic transfer parameters

	VD_B left	VD_B right	VD_C left	VD_C right	Mean	SD	CV
Z_{xfr} (MΩ), 0 Hz							
axon <−> soma	26	26	26	27	28	2.1	7%
axon <−> ipselateral far tip	27	26	28	27	29	2.6	9%
axon <−> contralateral far tip	25	25	26	26	27	2.4	9%
$\varepsilon_{axon,s}$ 0 Hz							
soma to axon	0.90	0.86	0.85	0.90	0.84	0.078	9%
ipselateral far tip to axon	0.91	0.86	0.92	0.91	0.85	0.094	11%
contralateral far tip to axon	0.85	0.83	0.84	0.87	0.81	0.089	11%
Z_{xfr} (MΩ), 100 Hz							
axon <−> soma	1.1	1.0	0.84	1.0	1.0	0.095	10%
axon <−> ipselateral far tip	1.2	1.1	2.2	1.2	1.4	0.5	34%
axon <−> contralateral far tip	0.82	0.84	0.81	0.81	0.83	0.184	22%
$\varepsilon_{axon,s}$ 100 Hz							
soma to axon	0.33	0.22	0.20	0.34	0.24	0.15	64%
ipselateral far tip to axon	0.38	0.24	0.52	0.38	0.33	0.20	61%
contralateral far tip to axon	0.26	0.19	0.19	0.26	0.21	0.15	72%

Transfer impedances (Z_{xfr}: MΩ) between key regions of two exemplar cells (VD_B and VD_C: columns 3-6), with mean values (column 7) for 5 cells (VD_E excluded). Attenuation factor may be calculated by dividing the transfer impedance between source and recording sites by the input impedance at the former (Table 1). "Conductance effectiveness" $\varepsilon_{axon,s} = Z_{transfer}/Z_{in,axon}$ provides an estimate for amplitude of a small (with respect to driving potential) PSP normalized to that for a synapse at the axonal site at 100 Hz. Ipselateral and contralateral "far" tips are the tips most

electrically distant from the axonal origin. Since values to ipselateral “near” tips are almost coincident with the axonal values, the far-tip values give a measure of the electrical extensiveness of the neuritic tree.

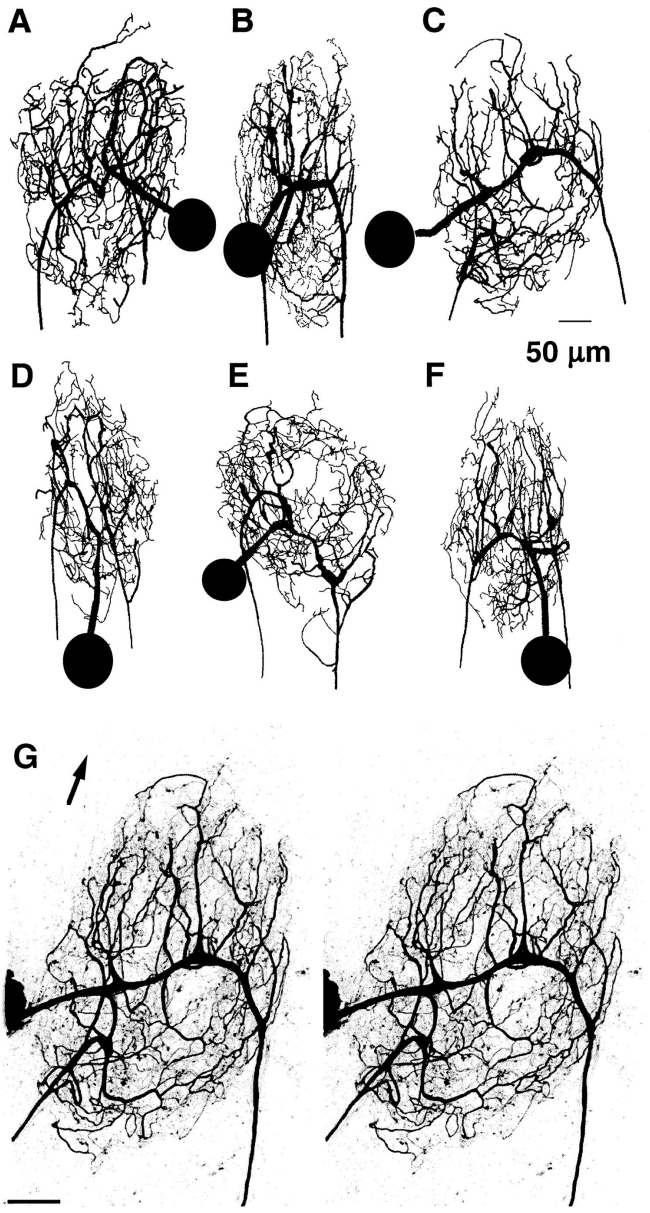

FIGURE 1. VD cells from the stomatogastric ganglion of a crab. A-F: Projections of 3D reconstructions of the 6 cells used in this study. Anterior direction up. Circular somata scaled to cell dimension have been superimposed on the projections. Letters in these panels are used to identify specific cells throughout the paper. G: Projections of the confocal microscope □stacks□ of optical sections through cell VDC presented as a stereo pair. Calibration bar: 50 □m. Arrow indicates anterior. These cells correspond to the following figures of Wilensky et al 2003: VDB= Fig. 2A, 3A, 4; VDC=Fig 2B, 3B; VDD = Fig. 2C, 3C.

128x234mm (300 x 300 DPI)

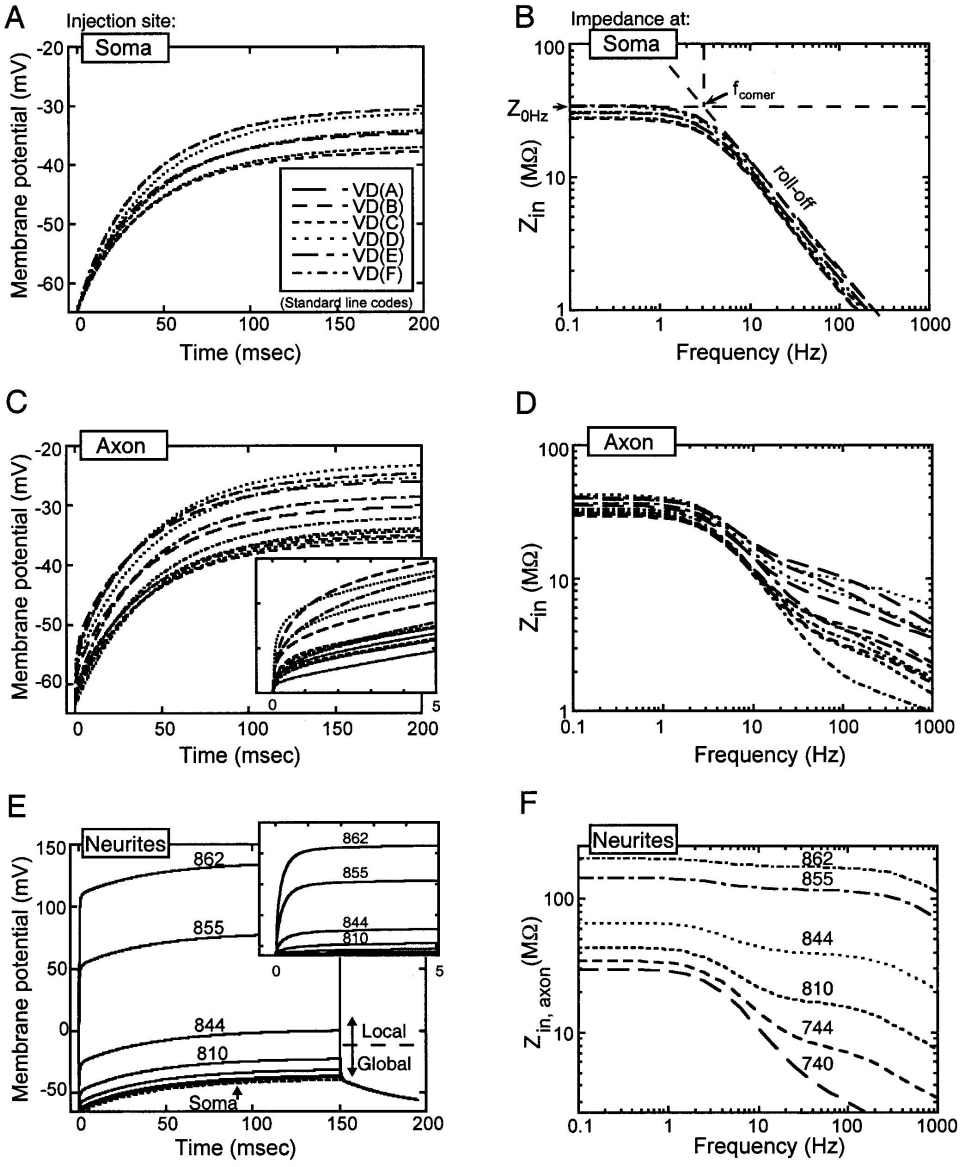

FIGURE 2. Input characteristics of VD cell regions. A. Simulated response for each of the 6 VD neurons of this study to 1 nA of depolarizing current injected into soma. Line codes apply to panels A-D. B. Bode plots for 6 VD cells, showing the amplitude of the voltage divided by the amplitude of impressed sinusoidal current as a function of frequency (log-log scale). Straight broken lines intersecting at the corner frequency (fcorner) show input impedance at 0 Hz (horizontal line; Z0Hz) and roll-off slope (diagonal line) for one of the cells. C. Input characteristics of axons. Voltage simulations for the points of origin (initial sections) of all 12 VD axons in response to a current step injected at the same point. Inset, first 5 ms of response (voltage scale □65 to □60 mV) showing variability in initial trajectory. D. Bode plot (log-log) for VD axons. Note variability in high-frequency

behavior. E. Simulated response to 1 nA current injected and recorded at sites spaced ca 50 □m along one secondary neurite trunk (the 6th most distal secondary from the soma along the left trunk, designated □ℓ6) of VDC. Trace numbering corresponds to sites labeled in Fig. 6A. Unnumbered traces (top to bottom): 744 and 740 respectively. Inset: expanded sweep: note very rapidly-rising (<1 msec) phase for distal points. F. Bode plots for the same sites in the secondary neurite of E. Note retention of high gain at high frequencies.

181x219mm (300 x 300 DPI)

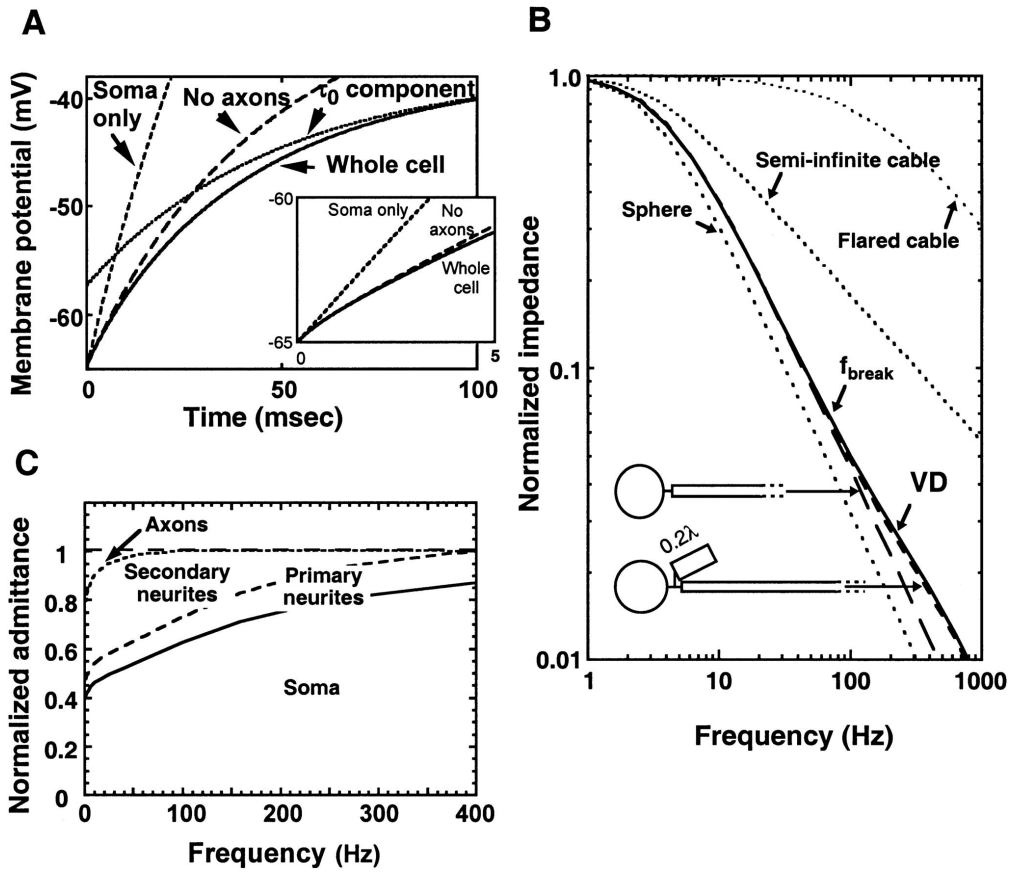

FIGURE 3. Details of soma input characteristics. A. Simulated response of a VD neuron (VDB) to 1 nA of depolarizing current injected into the soma. Solid line: trajectory for whole cell. Long-short broken line □no axons□ produced by removal of axons. Dashed line: □soma only□ produced by removal of all neurites. Top of frame represents asymptotic level for whole-cell trajectory; dotted line merging with whole-cell trajectory represents just the membrane time-constant component of charging (□0). Inset shows the initial 5 msec of the charging curve. B. Plots for simplified models approximating VD characteristics (see text). Broken line: sphere + infinite cylinder, the ratio of the DC input admittances 1:0.5 (sphere:cylinder) □dashed line: sphere + infinite cylinder + 0.2□ cylinder with admittance ratio 2:1:1. Dotted lines: extremes represented by sphere, semi-infinite cylinder and flared cylinder. The latter expands in diameter from 1 to 500 □m over 10 cm, approximating the 10-fold expansion of a VD process from distal neurite to axon over ca 200 □m. C. Normalized soma input admittance (=1/Zin) vs frequency plot (linear) for VDF showing effect of removing different regions of the cell. Normalized admittance for whole cell is defined as 1.0 at all frequencies (solid line). Broken line: removal of axons causes drop in admittance only at low frequencies. Dashed line: removal of secondary neurites. Dotted line: removal of primary neurites.
172x148mm (300 x 300 DPI)

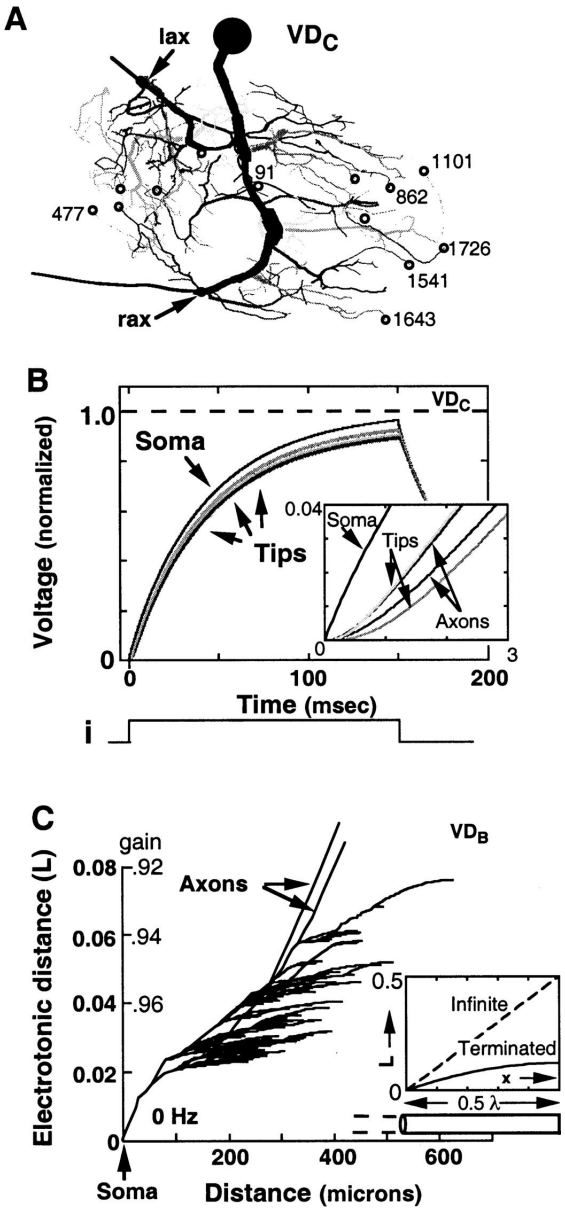

FIGURE 4. Electrotonic communication from soma to neurites. A. Diagram of standard tip sites of exemplar cell VDC. Each tip is from a different secondary and represents one of the longer paths through the secondary branch. lax = left axon origin; rax = right axon origin. Numbers serve as identifiers for electrode placements indicated in other figures. Unnumbered sites (left to right): 477, 1204 (below), 155, 1770, 737, 977, 1609. Site 643 overlies the left axonal origin. B. Simulated voltage recordings from neurite tips indicated in the diagram of Panel A in response to a 150 msec-long step of current injected in the soma; normalized to the asymptotic level reached in soma. Communication between soma and neurites is directional. From the soma out, DC attenuation is small and mostly confined to primary neurites. Inset shows initial trajectories for the soma, both axon

origins, and the two neurite tips from the standard set (Diagram in panel A) showing the most divergent trajectories (1609; 643). Note differences in delays. C. Dendrogram□ of electrotonic distance from soma to all parts of examplar cell VDB. (a unit electrotonic distance corresponds to an e-fold attenuation) for DC signals applied to soma (□gain□ scale: fractional signal remaining). Plotted as a function of physical distance from the soma (abscissa). Length constant of 3.7 □m-diameter axon-extensions = 2.8 mm.
88x190mm (300 x 300 DPI)

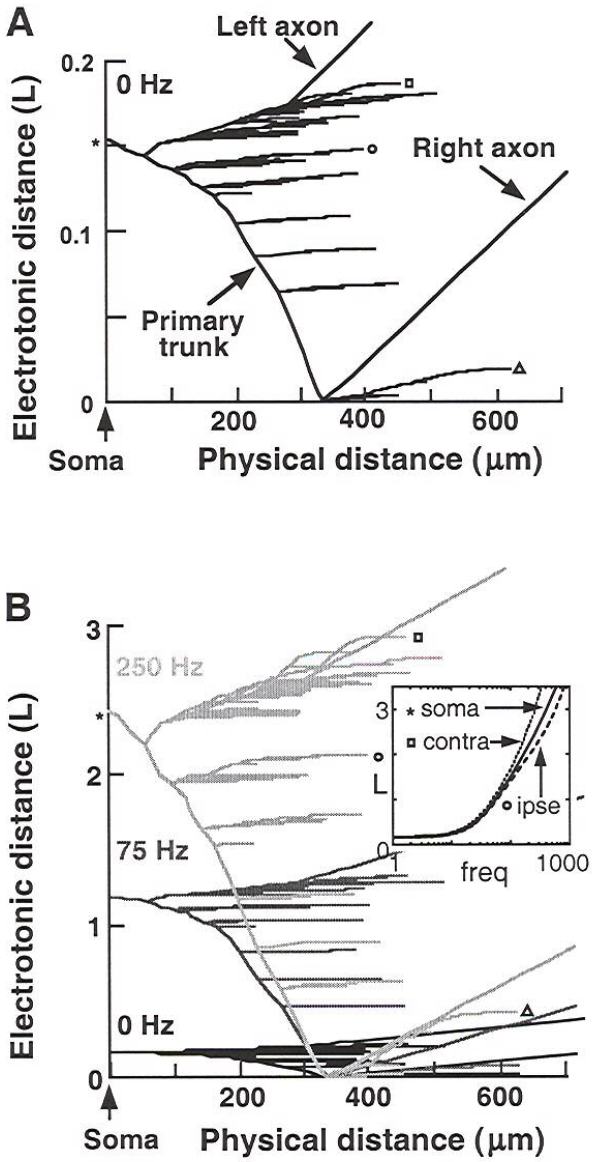

FIGURE 5. Electrotonic communication from axon origin to rest of cell. A. DC attenuation dendrogram showing electrotonic distance of the different points in the cell as a function of physical distance from the origin of the right axon (Cell VDB). B. Attenuation dendrogram for 3 frequencies: 0, 75, 250 Hz from the same location. Inset: Electrotonic distance (□L□) from the right axon origin as a function of frequency (log scale) for the soma (*) and two neurite tips, one from the left (contralateral) side (square symbol on main diagrams) and one from the ipselateral side (circle).
78x147mm (200 x 200 DPI)

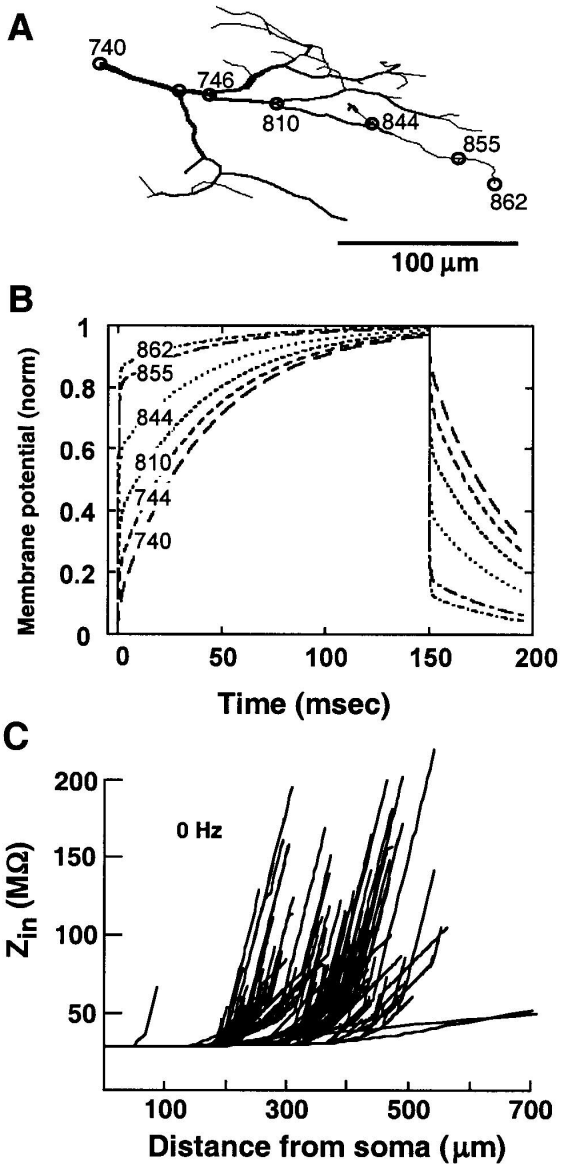

FIGURE 6 Input characteristics in neuropil. A. Secondary tree □ℓ6 (6th branch along left primary trunk) of exemplar cell VDC. Standard electrode sites for recording along the secondary trunk indicated by circles and numerical ID's. B. Normalized charging curves for current injected at locations indicated on diagram of Panel A and recorded from the same site. (VDC). Note the increasing dominance of the fast initial phase at more distal sites. C. Input impedance dendrogram for 0 Hz. Plot vs distance from soma. Parallel lines for the most distal neurites is an artifact of the pixel-based quantization of neurite diameter (multiples of 0.69 □m). (VDB)

87x177mm (300 x 300 DPI)

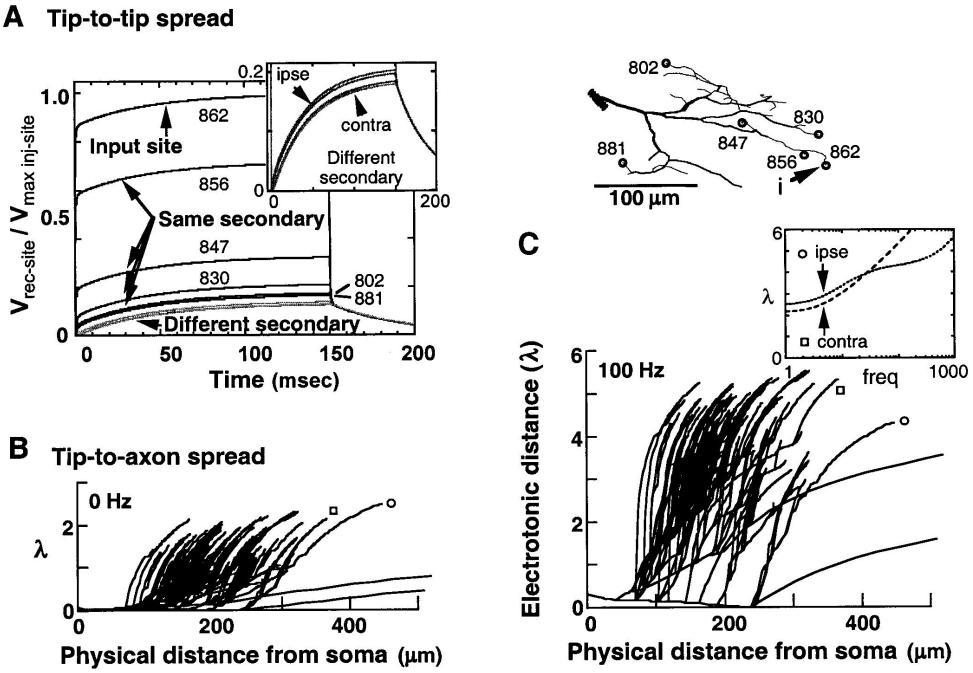

FIGURE 7. Electrotonic communication from neuropil to rest of cell. A. Charging trajectories in response to a long 1 nA current pulse injected into a left-side tip (862). Colored (/grey) traces: recording sites are from selected distal neurite tips arising from different secondary branches (see site diagram, Panel A, Fig 4). Black traces: sites along the same secondary trunk (diagram above: arrow □i" indicates injection site; circles recording sites). Voltages along the secondary axis rise abruptly, then more slowly as the whole cell charges (cf. Fig. 2E). Note that the fall-off in voltage with distance from the injection site is steep at first and lessens as the neurite diameter increases. Initial rapid phase of charging is more pronounced at more distal sites. Voltages at tips arising from each of the 12 non-shared secondary neurites are much smaller and lack the rapid component, illustrating tip-to-tip isolation across secondaries. There are slight differences between left-side and right side origins of the secondaries (inset). Zin, 0 Hz, 862 = 201 M□ B., C. Attenuation dendrograms for VDB from the various parts of the cell to the left axon (□conjugate□ diagrams to parts of Fig. 4). 0 and 100 Hz respectively. Inset shows frequency-dependence (log scale) of attenuation between two tips, one from each side (circle: ispelateral; square symbol: contralateral) to the origin of the left axon.
182x127mm (300 x 300 DPI)

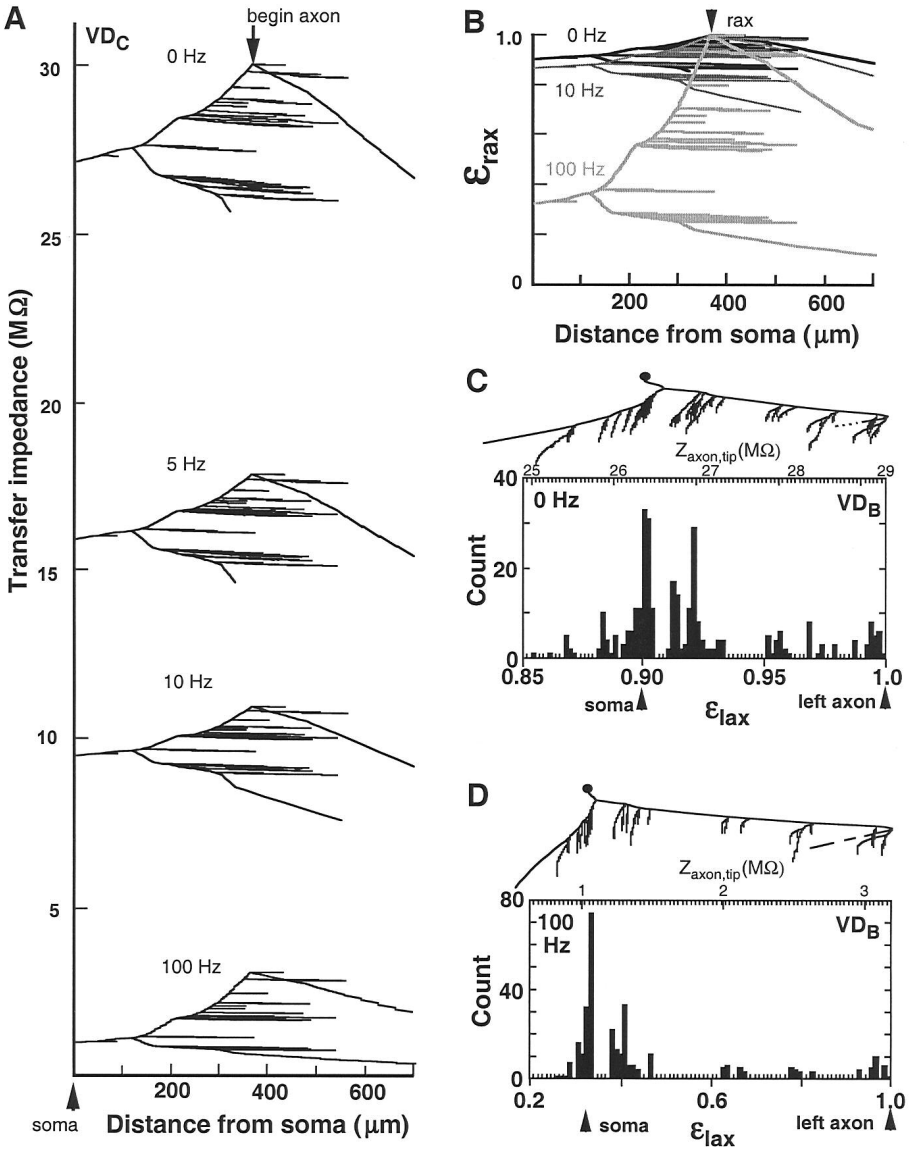

FIGURE 8. Transfer characteristics between axonal origins and other sites in VD. A. PSP's generated in VDC by alpha synapse (see caption to Fig. 12). Solid line: recording at the left axonal origin of PSP produced by synapse placed at a secondary tip (862, diagram in Fig 10A). Broken line: recording at tip 862 of PSP produced by synapse placed at left axonal origin. The PSP's superimpose because of reciprocity in the transfer impedance. Dotted lines: recordings at sites of synaptic input (□(862)□=tip; □(ax)□= left axonal origin). B. Impedance dendrograms at 0, 5, 10 and 100 Hz in VDC (top to bottom) with respect to the right axon origin. Left scale□: impedance magnitude (M□). Right scale: transfer impedance normalized to input impedance at axon origin for each frequency, representing □conductance efficacy:□ the voltage response amplitude expected at the

axon from a small sinusoidal conductance change at different points on the cell measured as a fraction of that produced by the conductance placed at the axon (see text). C. Transfer-impedance histograms at 0 Hz (upper panel) and 100 Hz for left axon origin (401) for exemplar cell VDB. Upper scale: impedance (M□); lower scale: □conductance effectiveness,□ □axon, relative to left axonal origin. Note histogram peaks corresponding to the different secondary trees (cf dendrograms above). Note that at the higher frequencies, secondary clusters are more segregated on the ipselateral side owing to steeper attenuation along the primary trunk (note change in vertical scale). Bin sizes: 0.05 M□ at 0 Hz; 0.03M□ at 100 Hz.

181x231mm (200 x 200 DPI)